

# High rate capability and cyclic stability of hierarchically porous Tin oxide (IV)–carbon nanofibers as anode in lithium ion batteries

Ashish Gupta<sup>1,3</sup> · Sanjay R. Dhakate<sup>1,3</sup> · P. Gurunathan<sup>2</sup> · K. Ramesha<sup>2</sup>

Received: 20 June 2017 / Accepted: 21 July 2017 / Published online: 29 July 2017  
© The Author(s) 2017. This article is an open access publication

**Abstract** Tin oxide–carbon composite porous nanofibres exhibiting superior electrochemical performance as lithium ion battery (LIB) anode have been prepared using electrospinning technique. Surface morphology and structural characterizations of the composite material is carried out by techniques such as XRD, FESEM, HR-TEM, XPS, TGA and Raman spectroscopy. FESEM and TEM studies reveal that nanofibers have a uniform diameter of 150–180 nm and contain highly porous outer wall. The carbon content is limited to ~10% in the nanofibers as shown by the TGA and EDAX which does not fade the high capacity of SnO<sub>2</sub>. These nanofibers delivered a higher discharge capacity of 722 mAh/g even after 100 cycles at high rate of 1C. The excellent electrochemical performance can be ascribed to the synergy effect of small amount of carbon in the composite and the hierarchically porous structure which accommodate large volume changes associated with Li-ion insertion–desertion. The porous nano-architecture would also provide a short diffusion path for Li<sup>+</sup> ions in addition to facilitating high flux of electrolyte percolation through micropores. The electrochemical performance of composite material has also been tested at 60 °C at a higher rate of

2C and 5C. Post cycling FESEM analysis shows no volumetric and morphology changes in porous nanofibers after completing rate capability at high rate of 10C.

**Keywords** Electrospinning · Nanofibers · Electrochemical performance · Cycle stability

## Introduction

Owing to the high energy density and long cycle life, rechargeable lithium ion batteries (LIBs) has drawn a great deal of attention as an energy source in portable devices such as mobiles, tablets and laptops. (Deng 2015; Reddy et al. 2013a). Further, LIBs can be seen as potential prospects for high end applications such as electric vehicles, renewable energy storage and grid support, if their power density could be amended substantially. The energy density of LIBs mainly depends on the electrode materials. Due to a number of materials being investigated as anode in LIBs (Cherian et al. 2013a; Jibin et al. 2012), there are lots of possibilities (Roy and Srivastava 2015). Presently, graphite (theoretical capacity ~372 mAh/g) is the commonly used anode material in commercial LIBs due to its good cyclability (van Schalkwijk and Scrosati 2007; Wu et al. 2003). However, poor intercalating rate capabilities and low specific capacity of graphite anode restrict its usefulness in high energy applications (Sivakkumar et al. 2010). Therefore, exhaustive research efforts are being carried out to identify a better electrode system such as alloying electrodes (Si, Sn, V etc.) and nanometric transition metal oxides (Cheng et al. 2016; Goriparti et al. 2014).

Although having high capacity, nevertheless, Sn and SnO<sub>2</sub> suffer from rapid decay in capacity (i.e. Poor cycle life) due to the volume change and pulverization of

✉ Sanjay R. Dhakate  
dhakate@nplindia.org

✉ K. Ramesha  
ramesha.cecri@gmail.com

<sup>1</sup> CSIR-National Physical Laboratory, Advanced Carbon Products, Dr. KS Krishnan Marg, New Delhi 110012, India

<sup>2</sup> CSIR-Central Electrochemical Research Institute-Chennai Unit, CSIR-Madras Complex, Taramani, Chennai 600113, India

<sup>3</sup> Academy of Scientific and Innovative Research (AcSIR), CSIR-NPL Campus, New Delhi, India

electrode during alloying–dealloying (Cherian et al. 2013b; Lou et al. 2009). To overcome these problems, two different approaches have been adapted by researchers to improve cyclability and maintain high capacity, first, to use nanostructured tin compounds (Cherian et al. 2013b) and second to use carbon–SnO<sub>2</sub> matrix (Wang et al. 2015) which acts as buffer to reduce the strain during lithiation–delithiation.

In this direction, Yang et al. have reported that size of SnO<sub>2</sub> nanoparticles play vital role in controlling the electrochemical performance (Yang et al. 2010). Park et al. demonstrated that morphology also play significant role (Park et al. 2008) in electrochemical performance of the electrode. A number of SnO<sub>2</sub> nanostructures with different morphologies have been fabricated such as nanoparticles (Deng and Lee 2008; Reddy et al. 2015) nanosheets (Ding et al. 2011), nanotubes (Um et al. 2015), nanowires (Jiang et al. 2009), microspheres (Gurunathan et al. 2014) and nanofibers (Hwang et al. 2014) to observe better electrochemical performance. Also various forms of carbon such as carbon nanotubes (Elizabeth et al. 2015), graphene (Liu et al. 2015; Zhang et al. 2015), amorphous carbon (Zhou et al. 2015) and crystalline carbon (Liu et al. 2012) have been used for preparing SnO<sub>2</sub>/carbon composites. The SnO<sub>2</sub>-based nanofibers having one dimensional structure have shown good performance as anode material in LIBs (Fu et al. 2014) due to several advantages like high surface area, easy handling, no agglomeration and tailored morphology.

Electrospinning is an inexpensive tool to form various polymeric nanofibers as well as composite nanofibers (Aravindan et al. 2015). These nanofibers can be converted into carbon nanofibers or ceramic nanofibers depending upon polymer, additives and heat treatment conditions. Numerous binary and ternary oxide materials with fibrous (Cherian et al. 2013a), nuggets (Viet et al. 2009) and rice morphology (Shengyuan et al. 2011; Zhu et al. 2012) has been synthesized using combination of electrospinning and heat treatment and found application as lithium ion battery materials. Selection of polymer plays important role in deciding morphology of nanomaterial after electrospinning. (Binitha et al. 2013) shows that chemical interaction of metal oxide precursor and metal oxide with polymer (as PVP) can lead to formation of nanofibers morphology but if there is no chemical interaction with polymer (as PVAc) it may evaporate leaving grains type structure. In case of PVP and PAN, both can form H-bonding with metal oxide and form nanofibers morphology. However, (Viet et al. 2009) show that heating temperature also have similar importance, despite of the polymer used. They have shown that Nb<sub>2</sub>O<sub>5</sub> nanofibers can retain their nanofiber morphology up to 800 °C, but results in nugget like morphology when heating up to 1100 °C due to melting of Nb<sub>2</sub>O<sub>5</sub>.

Polyacrylonitrile (PAN) polymer is conventionally used to make carbon nanofibers due to the high carbon content, high thermal stability and easy fabrication into nanofibers (Dhakate et al. 2011). PAN polymer can be used to form composite nanofibers with metal oxides, as by Yongzhi Wu et al., who fabricated NiO and RuO<sub>2</sub>-carbon composite nanofibers. These composite nanofibers proved to be used as electrode in both supercapacitors as well as lithium ion batteries (Wu et al. 2012).

Literature reports show that less thermally stable polymers such as PVAc (Xia et al. 2013) and PVP (Fu et al. 2014) have been used widely as sacrificing template for making SnO<sub>2</sub>-based nanofibers. In the study done by Hwang et al., electrospun nanofibers have been drawn from a mixture of PVP–SnCl<sub>2</sub> and heat treated at 750 °C to get pure SnO<sub>2</sub> nanofibers to use as anode material in LIBs. They have reported that electrochemical performance would vary depending upon the chemical composition and nanofibers geometry. Initial discharge capacity obtained for SnO<sub>2</sub> nanofibers anode is 1217 mAh/g at lower discharge rate of 0.1C, with a low columbic efficiency of 57%. Pure SnO<sub>2</sub> nanofibers show capacity of ~780 mAh/g at fiftieth cycle, however, only at a low discharge rate of 0.2C (Hwang et al. 2014). A list of literature reports on the synthesis of SnO<sub>2</sub> and SnO<sub>2</sub>-carbon nanofibers employing the electrospinning technique and their electrochemical performance are provided in Table 1 and compared with the present study (Bonino et al. 2011; Fu et al. 2014; Hwang et al. 2014; Jung and Lee 2011; Kim et al. 2014; Kong et al. 2012; Xia et al. 2012; Yang et al. 2015; Yang and Lu 2014; Yang et al. 2010; Zhou et al. 2014). In the present investigation, a facile (Wang et al. 2016), inexpensive route for the Synthesis of porous SnO<sub>2</sub>-carbon composite nanofibers with small amount of carbon using electrospinning technique has been developed. In literature, researchers have used stabilization and carbonization steps to form SnO<sub>2</sub>-carbon nanofibers (Zhou et al. 2014) and also some post treatment steps (Kong et al. 2012) which make process more complicated. But in our case PAN–SnCl<sub>2</sub> nanofibers were synthesized easily through electrospinning and converted into SnO<sub>2</sub>-carbon nanofibers via controlled heat treatment in air up to 600 °C. The material has shown promising results as anode material exhibiting good cyclability, capacity retention and rate capabilities.

## Experimental section

### Material preparation

Polyacrylonitrile with 6% methyl methacrylate (PAN copolymer) procured from RK Industries, UK and stannous chloride (Sigma Aldrich) were used as precursors for

**Table 1** Comparison of electrochemical performance of electrospun SnO<sub>2</sub> nanofibers reported in the literature with the present work

Material	Discharging rate	Initial capacity	Capacity (cycle)	References
SnO <sub>2</sub> @ carbon composite nanofibers	100 mA/g	966.5 mAh/g	420 mAh/g(100)	Yang et al. (2010)
	1C	650–700 mAh/g	~400 mAh/g(50)	
Pure SnO <sub>2</sub> nanofibers	100 mA/g	1069.1 mAh/g	334.1 mAh/g	
	1C		150 mAh/g	
Porous SnO <sub>2</sub> nanofibers	0.2C	~1200 mAh/g	~780 mAh/g (50)	Hwang et al. (2014)
SnO <sub>2</sub> -carbon nanofibers + SnSO <sub>4</sub> nanofibers	50 mA/g	788 mAh/g	470 mAh/g (40)	Bonino et al. (2011)
SnO <sub>2</sub> -carbon-NiO nanofibers	50 mA/g	–	60–110 mAh/g	Yang et al. (2015)
Sb doped SnO <sub>2</sub> nanofibers	100 mA/g	1350 mAh/g	~770 mAh/g (50)	Kim et al. (2014)
SnO <sub>2</sub> nanofibers	100 mA/g	1496 mA h/g	~500 mAh/g (50)	
SnO <sub>2</sub> @ carbon Nanofibers	80 mA/g	1375.5 mAh/g	508.9 mAh/g (50)	Fu et al. (2014)
SnO <sub>2</sub> Nanofibers		1815.3 mAh/g	334.1 mAh/g (50)	
Porous SnO <sub>2</sub> nanofibers	100 mA/g	1595 mAh/g	583 mAh/g (50)	Yang and Lu (2014)
	1000 mA/g		554 mAh/g (25)	
SnO <sub>x</sub> nanoparticles embedded carbon nanofibers (800 °C)	0.5 mA/cm <sup>2</sup>	1032 mAh/g	649 mAh/g (100)	Jung and Lee (2011)
		1956 mAh/g	57 mAh/g (100)	
SnO <sub>2</sub> nanoparticles			Nearly same as on 50	
SnO <sub>2</sub> nanoparticles@ carbon nanofibers	100 mA/g	1552.6 mAh/g	383 mAh/g (30)	Xia et al. (2012)
carbon/SnO <sub>2</sub> /carbon core-shell hybrid nanofibers	1C	~640 mAh/g	~600 (50)	Kong et al. (2012)
SnO <sub>x</sub> /carbon nanohybrid	0.5 A/g	1278 mAh/g	~570 mAh/g (50)	Zhou et al. (2014)
			608 mAh/g (200)	
Highly porous SnO <sub>2</sub> -carbon nanofibers	1C	2556 mAh/g	722 mAh/g (100)	Present work

electrospun nanofibers. PAN copolymer that is taken here as a source of carbon and Stannous chloride as a source for SnO<sub>2</sub>. *N,N*-dimethyl formamide (DMF) procured from Thomas Baker with 99% purity was used as solvent for both polymer and metal salt.

The experiment was performed as shown in schematic illustration (Fig. 1). Both stannous chloride and PAN copolymer (in the ratio 6:10) were dispersed in *N,N*-dimethyl formamide (DMF) using ultrasonication followed by continuous magnetic stirring (IKA C-MAG H7) at 30 °C for 8–10 h. Obtained homogeneous solution was then filled in three 5-ml syringes (0.55 mm needle dia) and electrospun to obtain bead-free nanofibers on aluminum foil wrapped on a rotating drum collector (2000 rpm) having a diameter of 16 cm. The voltage and flow rate were optimized at 15 kV and 0.2 ml/h to get the bead-free nanofibers. The nanofibers were peeled off easily in the form of white polymer sheet and calcined in air at 600 °C at heating rate of 300 °C/h and heated isothermally at 600 °C for 4 h to obtain highly porous SnO<sub>2</sub>-carbon composite nanofibers.

### Structural characterizations

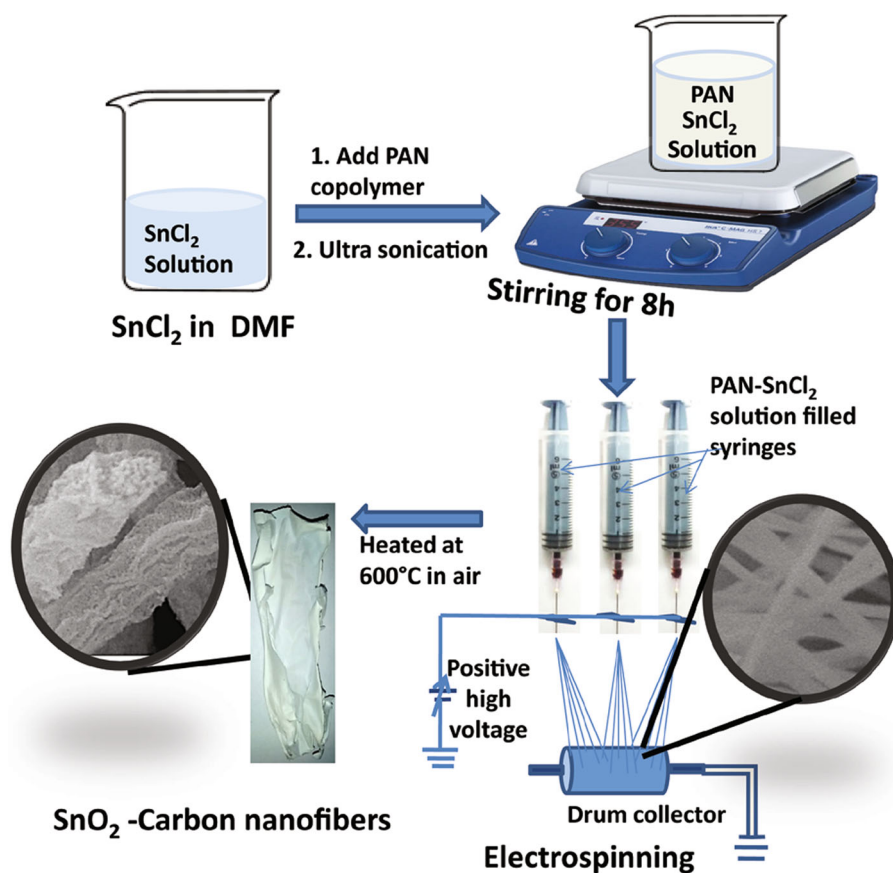
Morphological and elemental analysis of SnO<sub>2</sub>-carbon composite nanofibers was carried out using field emission scanning electron microscopy (FESEM, JEOL 7500FA)

and transmission electron microscope (TEM, JEOL 2200FS with Cs-corrector). Surface morphology of PAN-SnCl<sub>2</sub> nanofibers at various heating temperatures was analyzed through scanning electron microscope (SEM, EVO M-10). Thermo gravimetric analyzer (TGA, Mettler Toledo star system) was used to determine the carbon content in nanofibers and to detect characteristic changes in polymeric nanofibers during the heating process up to 600 °C. Raman study was performed using Renishaw inVia micro-Raman spectrometer with an excitation source of 514.5 nm ( $E = 2.41$  eV). X ray diffraction (XRD, Rigaku diffractometer Cu-K $\alpha$  radiation) studies were carried out to extract structural information of composite nanofiber. The chemical composition and functional groups present in the final nanofibers were analyzed by X-ray photoelectron spectroscopy (XPS, Thermo Scientific) using the monochromatic Al K-alpha source. The Brunauer-Emmett-Teller (BET) surface area measurements was carried out on Physisorption Analyzer (ASAP 2020, Micromeritics Instrument).

### Electrochemical measurements

The electrochemical performance of SnO<sub>2</sub>-carbon nanofibers was evaluated galvanostatically on CR2032 coin cells using VMP3Z Biologic multichannel battery testing

**Fig. 1** Schematic illustration of SnO<sub>2</sub>-carbon nanofibers fabrication



system. Working electrode was prepared by ball milling of 70% SnO<sub>2</sub>-carbon nanofibers with 20% SP-carbon. The ball-milled powder was mixed with 10% Na-Alginate binder and slurry was prepared using water as a solvent. The slurry was coated on 15 μm thick Cu foil. The electrode was dried in oven at 100 °C for 12 h to remove moisture. After that, electrode was cut into circular discs (16 mm dia) for cell testing. The geometrical area of the electrode is 2.00 cm<sup>2</sup>. The electrodes were assembled in a glove box (Ar filled) using pure Li foil as counter and reference electrode. A porous polypropylene (Celgard) used as a separator and 1.0 M LiPF<sub>6</sub> in ethylene carbonate (EC)/diethyl carbonate (DEC)/dimethyl carbonate (DMC) (2:1:2 by volume) was used as the electrolyte for cell testing. Cyclic voltammetry (CV) measurements were carried out at a scan rate of 0.1 mV/s between 0.01 and 2.0 V at room temperature. The charge-discharge cycling was carried out between 0.01 and 1.2 V potential window. The mass of active material (SnO<sub>2</sub>-carbon nanofibers) loading typically around 3.0–4.0 mg/cm<sup>2</sup> was measured by ultra-micro analytical balance. Electrochemical impedance studies were performed in the frequency range of 400–10 MHz with a perturbation of 20 mV applied versus Li/Li<sup>+</sup> at room temperature. EIS Data were recorded during discharge state at various voltages in the range of

2.9–0.01 V. At each voltage, during discharging state the cell was exposed to a current density of 100 mA/g and the cells were kept at rest at the given voltage for half an hour before recording the spectra, EIS data have been fitted using Zsimpwin software.

## Result and discussion

### Thermal analysis of nanofibers

Figure 2 shows the TGA curve of PAN-SnCl<sub>2</sub> nanofibers in the temperature range 30–700 °C heated in air atmosphere. The data shows three main weight loss areas, the rectangular marks in curve show the initiation temperature of weight loss. The first small weight loss occurs from 40 to 100 °C is due to the loss of moisture.

The second weight loss around 170 °C is attributed to decomposition of SnCl<sub>2</sub> in air (Kong et al. 2011). The major weight loss occurs between 450 and 640 °C which is due to the evaporation and rapid decomposition of carbon and other constituents from PAN copolymer. Also, at the same temperature the SnCl<sub>2</sub> gets converted into SnO<sub>2</sub>. However, After 640 °C, there is negligible weight loss which reveals that some stable compound formed which



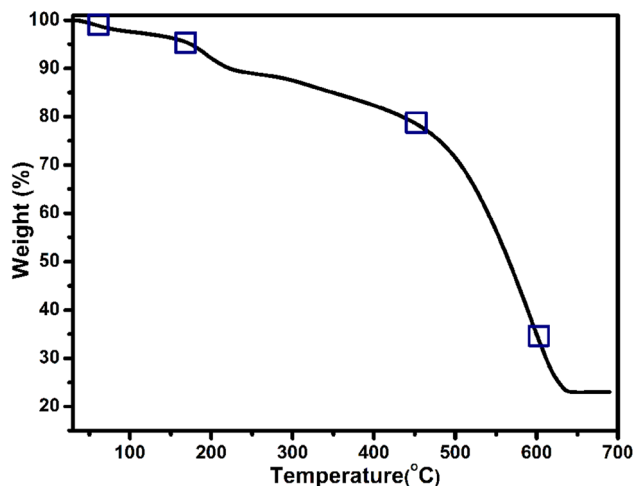


**Fig. 2** TGA graph of PAN-SnCl<sub>2</sub> nanofibers in air

should be SnO<sub>2</sub>. We have heated nanofibers only up to 600 °C so that some amount of carbon must be present that forms SnO<sub>2</sub>-carbon composite. Between the temperature 600 and 640 °C, there is wt loss of approximately 11% which may be due to loss of residual carbon. So, on heating the composite nanofibers at 600 °C, ~11% carbon remains in final morphology. The presence of carbon confirmed by EDAX is depicted in inset of Fig. 3d.

### Morphology and elemental analysis of nanofibers

The SEM analysis combined with TGA data was used to trace out a possible mechanism for SnO<sub>2</sub> nanofibers formation during heat treatment. Figure 3 shows the SEM

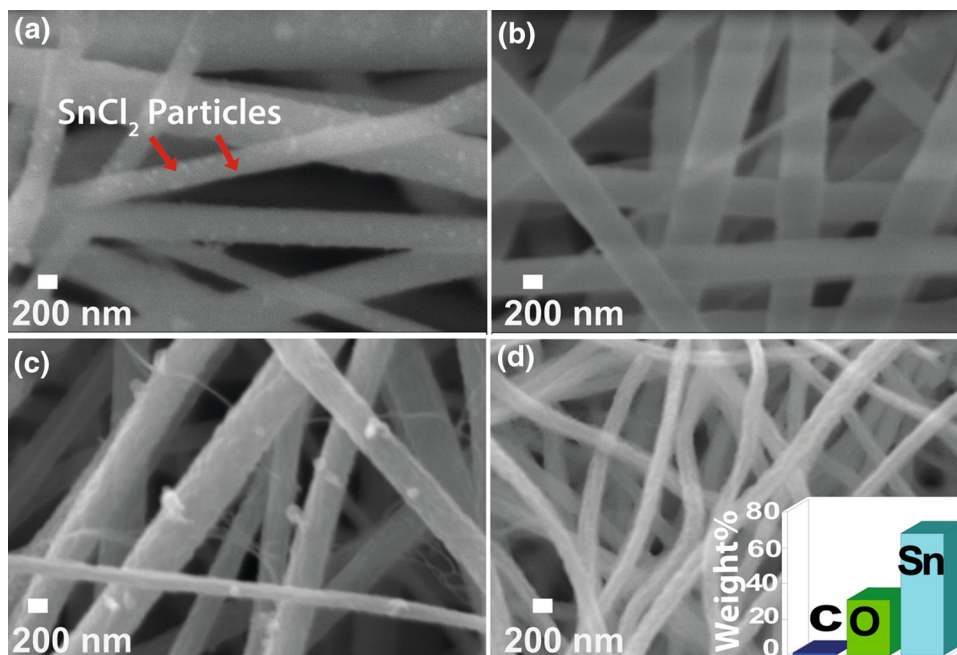
images of as such electrospun nanofibers and heat treated nanofibers, the intermediate temperature for heat treatment was identified from the TGA curve. Figure 3a shows the SEM image of pristine PAN-SnCl<sub>2</sub> nanofibers having diameter in the range 350–500 nm. The image also shows the presence of fine nanosized particles distributed on the surface of nanofibers which are probably SnCl<sub>2</sub> nanoparticles. When heated to 170 °C, the SnCl<sub>2</sub> particles present on nanofibers surface diffuse into PAN fibers and disappear from the nanofibers surface (Fig. 3b).

At higher temperatures (above the melting point) due to concentration gradient SnCl<sub>2</sub> diffuses to the surface having carbon in the core, making core-shell type structure, however, no change in diameter was observed. On further heating to 450 °C, the SEM shows porous surface formation due to the evolution of CO<sub>2</sub> during the decomposition of carbon from the fiber matrix (Fig. 3c). Some particles are seen on the surface of 450 °C heated nanofibers might be due to the crystallization of surfaced SnO<sub>2</sub>. At this stage, due to decomposition, SnCl<sub>2</sub> will get converted into SnO<sub>2</sub> nanocrystals (Kamali et al. 2014). Figure 3d shows the SEM image of 600 °C heat-treated PAN-SnCl<sub>2</sub> nanofibers. The image shows the formation of hierarchical porous nanofibers in a self supporting network having a diameter in the range 150–180 nm.

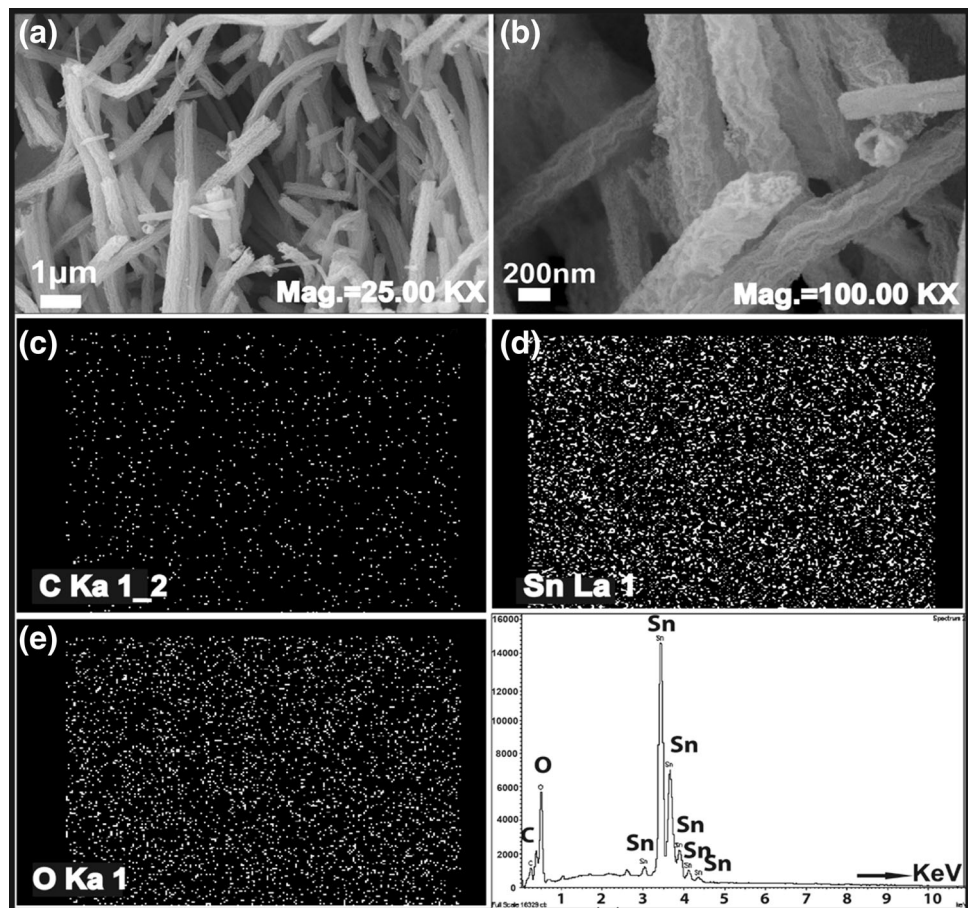
It can be perceived from the TGA curve that the carbon content in the 600 °C heated sample is around 11% (also detected by EDAX, XPS, XRD and RAMAN analysis) (Fig. 3d inset).

Figure 4 shows the FESEM images of SnO<sub>2</sub>-carbon nanofibers formed after heat treatment at 600°C. Figure 4a,

**Fig. 3** PAN-SnCl<sub>2</sub> nanofibers **a** as such **b** heated at 170 °C, **c** heated at 450 °C, **d** at 600 °C (Magnification 50KX) (inset EDAX data)



**Fig. 4** FESEM analysis of SnO<sub>2</sub> nanofibers **a** low magnification, **b** high magnification and elemental mapping **c** carbon, **d** Tin, **e** Oxygen, **f** EDAX plot

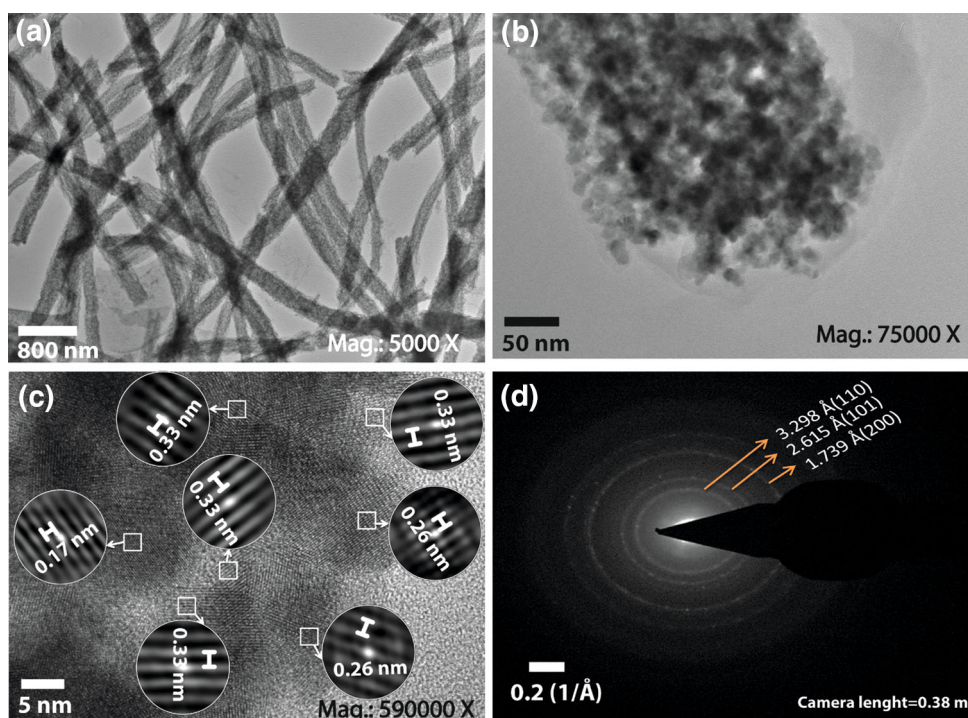


b shows low and high magnification images, respectively, which clearly shows mesoporous structure of SnO<sub>2</sub>–carbon nanofibers. The elemental mapping of nanofibers sheet (shown in Fig. 4a) in the area  $13 \times 10 \mu\text{m}$  was performed using the elemental analysis technique attached to FESEM. The elemental mapping of SnO<sub>2</sub>–carbon nanofibers reveals the presence of C, Sn, and O (Fig. 4c–e) which was also confirmed by XPS later. As can be seen, the carbon is found in least amount, but distributed evenly in all fiber areas while Sn is present in highest amounts with oxygen that is due to the presence of SnO<sub>2</sub>. Figure 4f shows EDX plot for nanofibers displaying the presence of C, Sn and O elements.

Figure 5 shows TEM and HRTEM images of porous SnO<sub>2</sub>–carbon nanofibers. Figure 5a shows porous structure of SnO<sub>2</sub>–carbon nanofibers with uniform tube diameter of 150–180 nm. In the nanofibers, the darker regions indicate presence of SnO<sub>2</sub> nanocrystals while the brighter spots designate pores formed during the evolution of carbon dioxide from the surface during heat treatment at 600 °C in air atmosphere. Figure 5b shows a higher magnification (75000X) TEM image of single SnO<sub>2</sub>–carbon nanofiber. It

clearly shows that the single nanofiber comprises of closely packed SnO<sub>2</sub> nanocrystals having voids. The nanofibers have diameter nearly 190 nm. Also, some void space can be seen in between SnO<sub>2</sub> nanoparticles in nanofiber which shows porous nature of nanofibers and may also help in compensating volume changes during alloying–dealloying. The nanoparticles size varies from 4 to 5 nm were calculated using image J analysis software. The HRTEM image Fig. 5c of the nanofibers shows the presence of different phases of SnO<sub>2</sub>. The lattice planes observed at seven different places were selected and auto correlated using Gatan software and the d-spacing is measured, labeled for the respective planes observed, using Gatan software using auto correlation with respect to the scale and depicted in the Fig. 5c. The measured d-spacing corresponds to the different planes of rutile SnO<sub>2</sub> structure, i.e., 3.3 Å (110) and 2.6 Å (101). The SAED shows the quasi polycrystalline nature of SnO<sub>2</sub>–carbon nanofibers in the form of clear ring formation (Fig. 5d). The d-spacing measured 3.3, 2.6 and 1.73 Å corresponds to (110), (101) and (200) planes which is in agreement with XRD and HRTEM results.

**Fig. 5** SnO<sub>2</sub>–carbon nanofibers **a** TEM images at low magnification, **b** TEM images at high magnification, **c** HRTEM images with calculated fringes in nm, **d** SAED pattern



### XRD pattern and Raman spectroscopic analysis of SnO<sub>2</sub>–carbon composite nanofibers

XRD pattern of SnO<sub>2</sub>–carbon nanofibers sample shown in Fig. 6a confirms the polycrystalline nature of SnO<sub>2</sub> in the composite nanofibers. The XRD pattern matches well with the standard rutile SnO<sub>2</sub> pattern (JCPDS#41-1445) with tetragonal space group P42/mnn and lattice parameters;  $a = 4.738$ ,  $b = 4.738$  and  $c = 3.187$  Å. Crystallite size calculated from peak at  $2\theta = 33^\circ$  (101 plane) is found to be  $<5$  nm. Due to much lower amount of carbon, no sharp peak was observed, but a broad hump between  $2\theta$  values of  $18^\circ$  and  $23^\circ$  indicating presence of amorphous carbon was observed.

Figure 6b shows the Raman spectra for SnO<sub>2</sub>–carbon nanofibers. In the tetragonal rutile structure, Sn<sup>4+</sup> ions are surrounded with six O<sup>2-</sup> ions in the unit cell. The active Raman modes were observed at 137, 488, 633.6 and 776.06 cm<sup>-1</sup> corresponds to B<sub>1g</sub>, E<sub>g</sub>, A<sub>1g</sub>, and B<sub>2g</sub> vibration modes of SnO<sub>2</sub>, respectively. The strongest intensity peak of A<sub>1g</sub> mode is characteristic of SnO<sub>2</sub> structure. A<sub>1g</sub> along with B<sub>2g</sub> mode corresponds to the expansion and contraction vibration mode of Sn–O bonds. The presence of these two modes establishes the presence of tetragonal rutile structure of SnO<sub>2</sub>. E<sub>g</sub> and B<sub>1g</sub> modes do not appear in the bulk SnO<sub>2</sub> but seen only in case of nanocrystals, however, with low intensity. With decreasing size, relaxation of  $k = 0$  selection rule is progressive and IR modes becomes weakly active due to the structural changes

induced by defects or disorders and size effects. Thereby E<sub>g</sub> and B<sub>1g</sub> related to the IR active A<sub>2u</sub> mode (720 cm<sup>-1</sup>) and IR-active E<sub>u</sub> (313 cm<sup>-1</sup>) TO mode, due to the nanostructured SnO<sub>2</sub> (Dieguez et al. 2001). The prominent peak of S1 arises due to the small particle size of SnO<sub>2</sub>. Also, a weaker peak at 1349 cm<sup>-1</sup> with much lower intensity corresponds to carbon was also detected, showing the presence of a small amount of carbon in the final SnO<sub>2</sub>–carbon nanofibers.

### XPS study of SnO<sub>2</sub>–carbon nanofibers

The surface chemistry of nanofibers is investigated by XPS. Figure 7a shows the XPS spectra obtained for SnO<sub>2</sub>–carbon nanofibers in general, revealing the presence of carbon, tin and oxygen. The general spectra evaluation shows no extraneous elements detected as an impurity. The peaks for Sn 4d, 4p, 4s, 3d, 3p and 3s are observed for SnO<sub>2</sub> in the general spectra.

Figure 7b shows the deconvoluted XPS peaks of C1 s in the binding energy range 278–300 eV with major peak at 284.1 eV for C–C. The two other small peaks at 285.6 and 287.95 eV may be attributed to the formation of C–O–C, and O–C=O due to exposure to air. The presence of Sn3d<sub>5/2</sub> and Sn3d<sub>3/2</sub> peaks, respectively, at 486 and 494.4 eV for Sn<sup>4+</sup> with a peak difference of 8.4 eV is shown in Fig. 7c. Peak near 498 eV may be due to some chemisorbed OH or dissociated oxygen on the surface. Figure 7d shows deconvoluted peaks for O1s (oxygen) in the binding energy



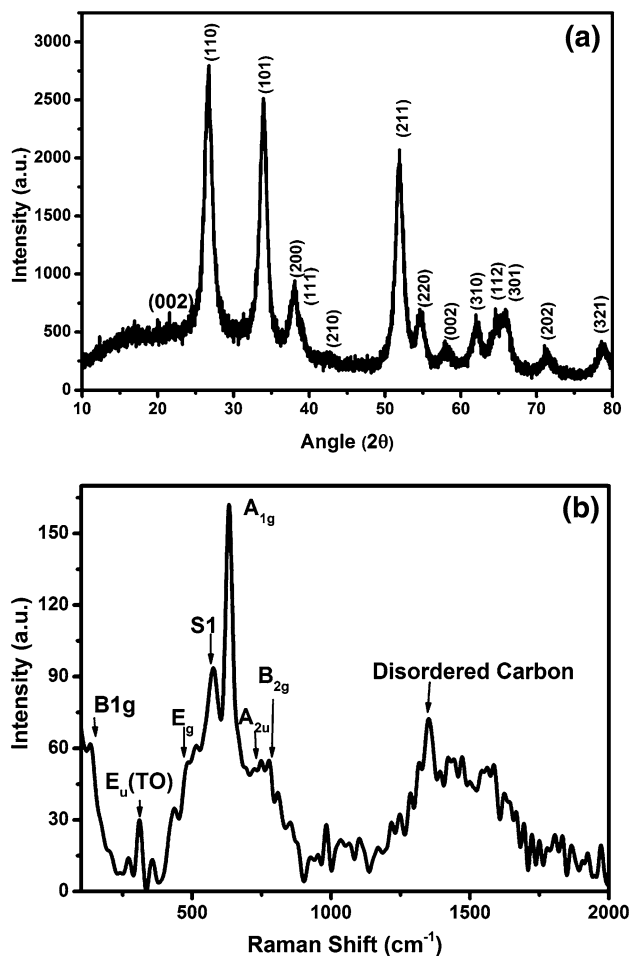


**Fig. 6** a XRD and b Raman analysis of SnO<sub>2</sub>-carbon nanofibers

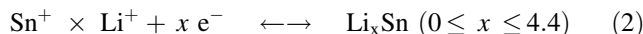
range 524–540 eV. The peak at 530.1 eV mainly attributed to metal oxides, while two peaks at 532 and 534.3 eV are attributed to some C–O or C=O bonds formed due to atmospheric exposure as stated above.

### Surface area analysis

Figure 8 shows the curve between the relative pressure and quantity of N<sub>2</sub> gas adsorbed in nanofibers at standard temperature and pressure. The BET surface area is found to be 20.99 m<sup>2</sup>/g, which is higher than the similar nanofibers having surface area 13.48 m<sup>2</sup>/g (Hwang et al. 2014). inset of Fig. 8 shows the graph between pore diameter and pore volume incremental, i.e., pore size distribution along with increasing pore volume. The maximum pore volume of 0.014 cm<sup>3</sup>/g was observed for the pore diameter of 16.5 nm. BJH adsorption pore volume of 0.121 cm<sup>3</sup>/g, pore size distribution from ~1.7 to 300 nm with BJH average pore diameter 22.84 nm and BET average pore width 24.42 nm was observed, which shows the highly porous nature of nanofibers.

### Electrochemical analysis of SnO<sub>2</sub>-carbon nanofibers

We investigated the potential use of SnO<sub>2</sub> carbon nanofiber as anode material for lithium ion batteries. We have carried out cyclic voltammetry (CV) studies in the potential window of 0.01–2.0 V at a scan rate of 0.1 mV/s as depicted in Fig. 9a for initial five cycles. During the first cathodic scan an irreversible reduction peak with a maximum at 0.76 V is seen which is attributed to the reduction of SnO<sub>2</sub> to metallic Sn and the formation of the solid electrolyte interphase (SEI) layer in the first cycle Eq. (1) (Ding et al. 2014; Reddy et al. 2013a, 2015; Yim et al. 2011; Zhu et al. 2011).



This peak disappears in the following cycles. The cathodic peak located at 0.12 V is due to the formation of the Li<sub>x</sub>Sn alloy phase (0 ≤ x ≤ 4.4) (Eq. 2). The anodic peaks observed in the first cycle at 0.13, 0.54 and 1.26 V corresponding to Li extraction, de-alloying of Li<sub>x</sub>Sn and the partially formation of SnO<sub>x</sub>, respectively, as reported in the literature (Ding et al. 2014). In subsequent cycles, the peak at 0.76 V is separated into two peaks (about 0.62 and 0.92 V), that can be ascribed to the formation of the solid electrolyte interphase (SEI) and the tin oxide reduction to metallic tin. During charge cycles de-alloying of Li<sub>x</sub>Sn to Sn occurs below 1 V.

If we cycle higher than 1 V during charging cycles, conversion reaction gets activated, Sn–SnO (~1.2 V) and SnO–SnO<sub>2</sub> (>1.8 V). We have cycled SnO<sub>2</sub>-carbon nanofibers in the voltage range 0.01–1.2 V. So some extent of partial conversion reaction (Sn–SnO) could be anticipated (Ding et al. 2014; Reddy et al. 2013a, 2015; Yim et al. 2011; Zhu et al. 2011).

The charge–discharge curves for 1st, 10th, 25th, 40th, 50th, 70th and 100th cycles at 1C rate is shown in Fig. 9b. Current density value for 1C is (790 mA/g). The capacity (charge and discharge) values obtained are as follows: for 1st cycle (868 and 2556 mAh/g), 10th cycle (830 and 841 mAh/g), 25th cycle (810 and 815 mAh/g), 40th cycle (797 and 800 mAh/g), 50th cycle (780 and 786 mAh/g), 70th cycle (751 and 759 mAh/g) and 100th cycle (720 and 722 mAh/g), respectively. The high discharge capacity at first cycle may have two reasons.

First, Eq. (1) indicates a complete reduction of SnO<sub>2</sub> takes 4 Li<sup>+</sup> and in the (2) step, 4.4 Li<sup>+</sup> for the alloying process. From reaction 1 and 2, it is clear that the first discharge involves total 8.4 Li which amounts to high discharge capacity. Second, the larger than the expected capacity in the first discharge is also due to the electrolyte decomposition in the low potential region, resulting in



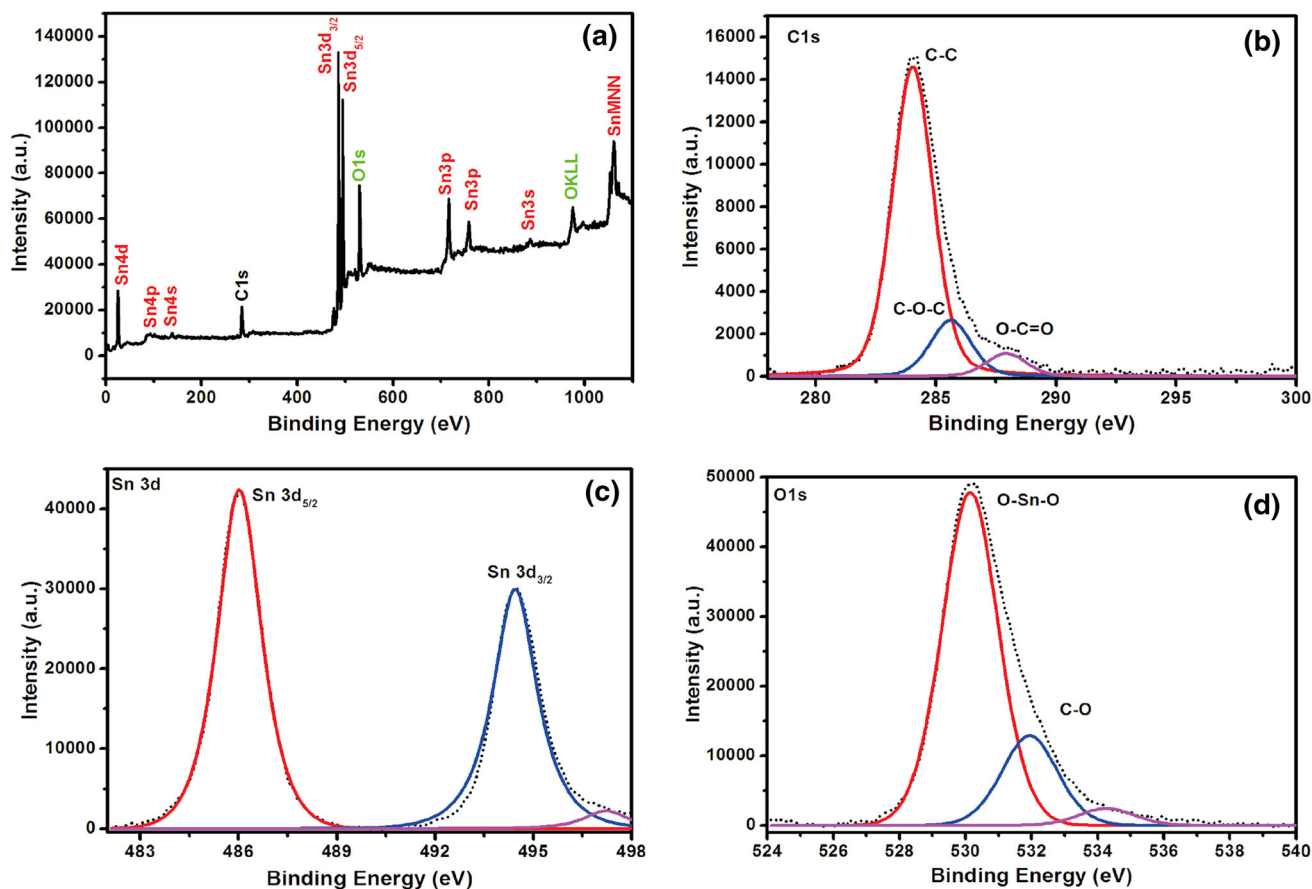


Fig. 7 XPS spectra of a general, b C1 s spectrum, c Sn 3d, d O1s in SnO<sub>2</sub>-carbon nanofibers

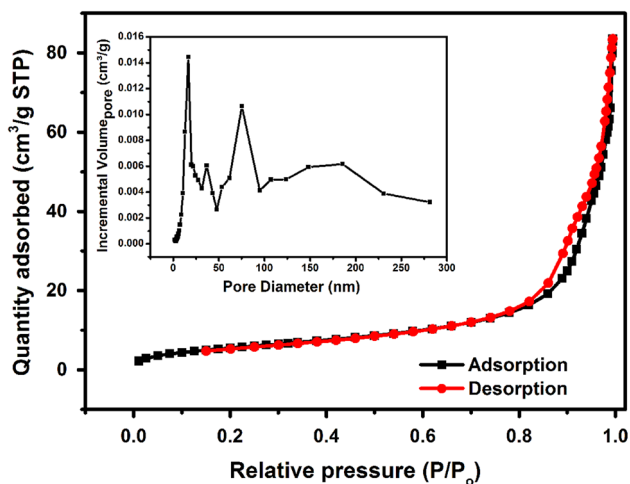


Fig. 8 BET Adsorption and desorption isotherms of SnO<sub>2</sub>-carbon nanofibers (inset) pore volume Vs pore diameter curve

formation of SEI layer on the surface of Sn/C composite matrix (Zhu et al. 2011). This also adds up to the first cycle irreversibility and low coulombic efficiency. In subsequent cycle expected reversible capacity is ~790 mAh/g.

Figure 9c shows the discharge capacity and coulombic efficiency curve with respect to cycle number. After 100

cycles 88% of capacity retention is seen even at high discharge rate of 1C. The constant capacity at such high rate may be attributed to the composite structure, the presence of carbon as well as the porous structure as all aspects will contribute to alleviating the volume expansion and strain relaxation. In our previous studies (Gurunathan et al. 2014) it was shown that Na-alginate binder increases the ionic conductivity during charging and discharging which enables high specific discharge. The average capacity obtained for SnO<sub>2</sub>-carbon composite at 1C rate is 750 mAh/g. From this, it is clear that the SnO<sub>2</sub>-carbon composite reported here exhibits superior electrochemical performance in terms of capacity retention, rate capability, discharge capacity and coulombic efficiency with respect to cycle number.

Electrochemical impedance spectroscopy (EIS) was used further to probe charge transport kinetics of the composite electrode. Figure 9d compares Nyquist plots of the SnO<sub>2</sub>-carbon nanofiber electrode before electrochemical cycling, after 2nd discharge and after 50th cycle. The impedance plots show one compressed semicircle in the medium frequency region, which could be assigned to charge-transfer resistance ( $R_{ct}$ ) and inclined line which corresponds to the lithium diffusion kinetics in the low-

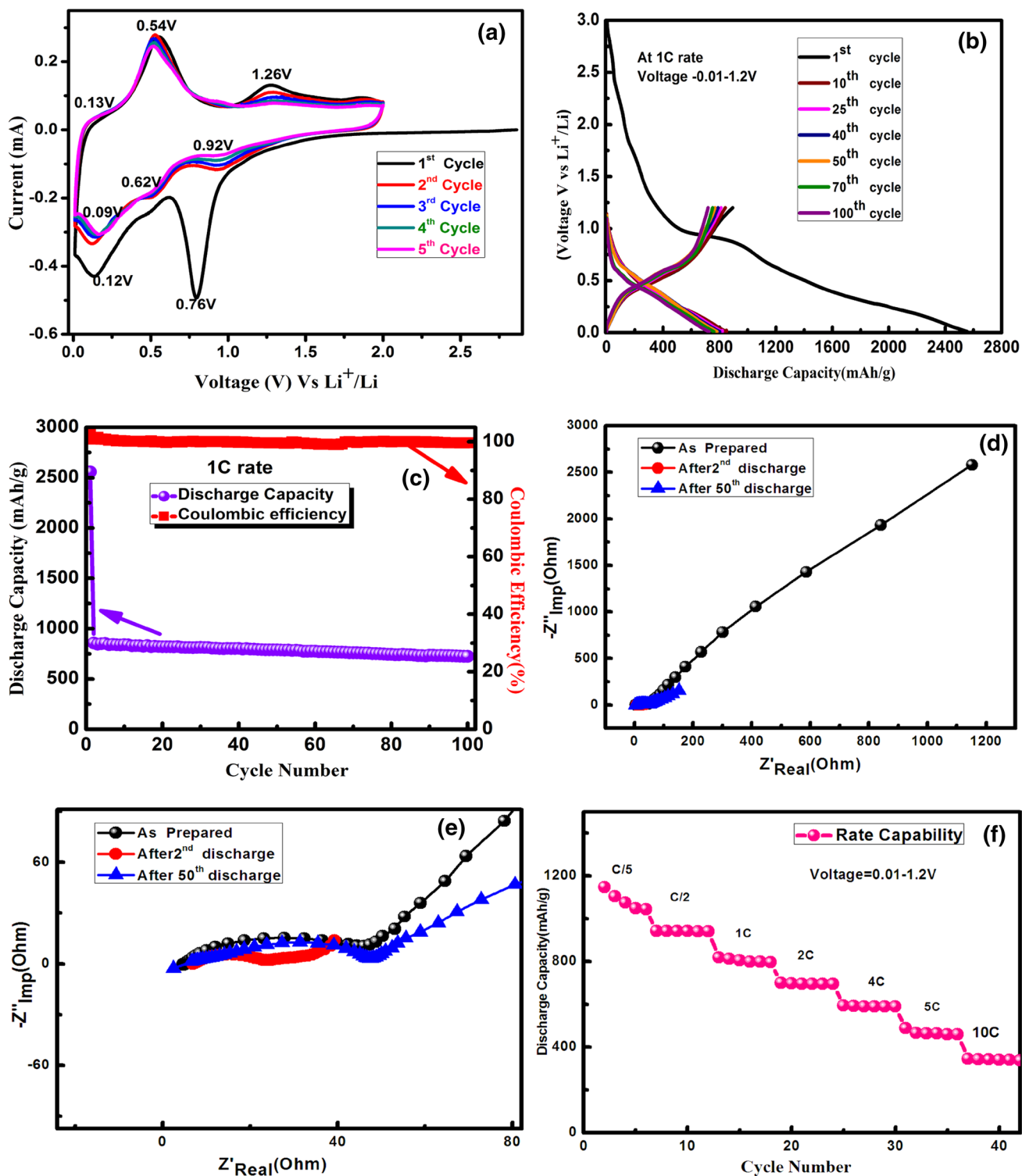


**Fig. 9** Electrochemical analysis of SnO<sub>2</sub>-carbon nanofibers **a** cyclic voltammogram (CVs) within the voltage range of 2.0–0.01 V at 0.1 mV/s scan rate, **b** charge–discharge Vs Voltage curve, **c** cycle

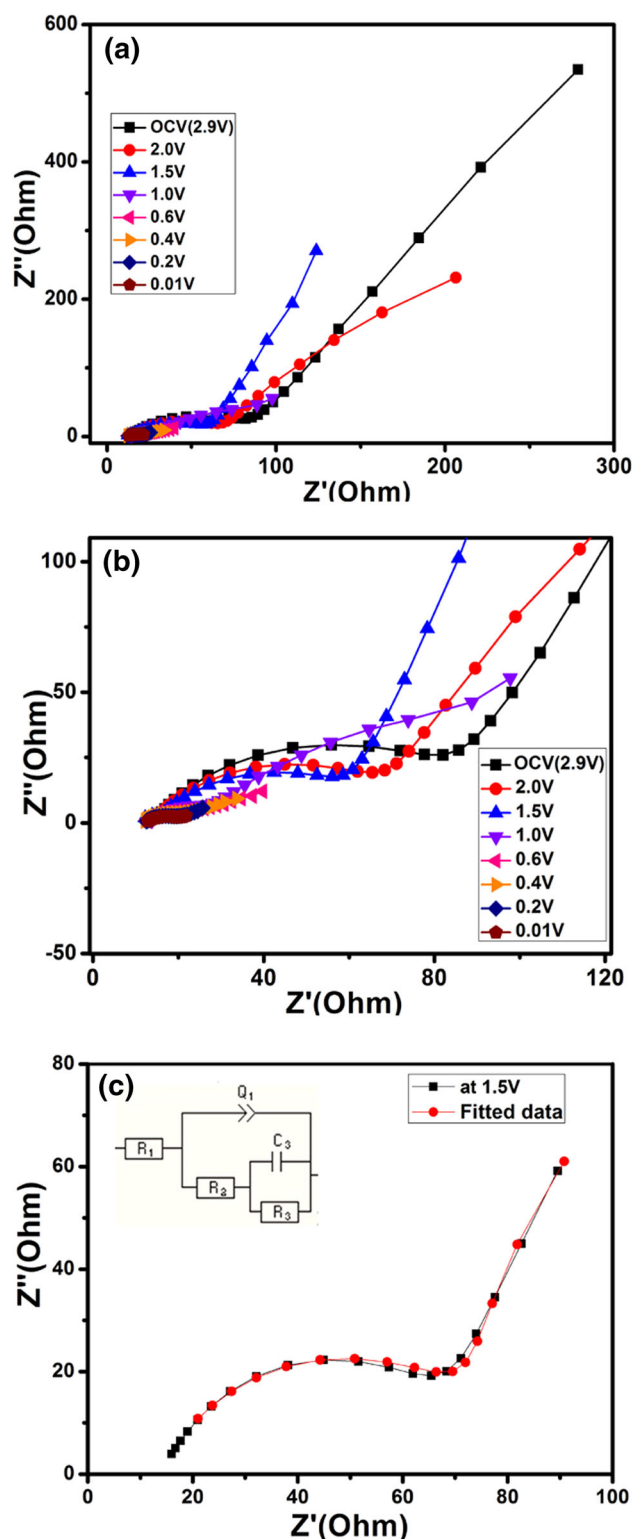
number Vs discharge capacity plot, **d** electrochemical impedance spectra (EIS), **e** enlarged view of EIS, **f** rate capability curve at different discharge rates

frequency range considered as Warburg impedance ( $W_z$ ). Figure 9e shows enlarged EIS spectra, after 2nd cycle,  $R_{ct}$  value is lower than that of fresh electrode, indicating the enhanced electron transfer due to the good conductivity of electrode. After 50 cycles, the  $R_{ct}$  value slightly increased, indicating an increase in electrode resistance due to the SEI layer formation.

Figure 9f shows the discharge capacity of composite nanofibers at different discharge rates which determine the rate capability of  $\text{SnO}_2$ -carbon nanofibers. The discharge capacity at C/5, C/2, 1C, 2C, 4C, 5C and 10C were found to be around 1050, 942, 860, 720, 640, 465 and 341 mAh/g, respectively. Capacity retention is good at all the rates proving that the volume expansion issue has been overcome by the composite structure resulting in good electrode stability. Also, the nano-architecture facilitates fast  $\text{Li}^+$  mobility leading to high power density.

Figure 10a gives the Electrochemical impedance spectra (EIS) for  $\text{SnO}_2$ -carbon nanofiber at different discharge potentials (2.9–0.01 V). The discharge impedance plot shows a single semicircle, which corresponds to  $R_{(sf + ct)}$  and CPE ( $sf + dl$ ). This is because the passage of current through the cell gives rise to  $R_{ct}$ . Furthermore, the EIS data have been fitted using Zsimpwin software using the equivalent circuit shown in the inset of Fig. 10c. In the equivalent circuit,  $R_s$  represents the solution resistance,  $R_{s1}$  is the resistance of SEI layer,  $R_{ct}$  is the charge-transfer resistance,  $W$  represents the Warburg resistance and CPE1 and CPE2 represent the double layer capacitance and capacitance of passivation film, respectively. During discharging the resistance values leads to decreased as reported literature (Cherian et al. 2013b; Nithyadharseni et al. 2015; Reddy et al. 2013b, 2011). The resistance values are moderately low, which indicates that good Li-ion kinetics at given voltages. The values of  $R_s$ ,  $R_{s1}$  and  $R_{ct}$  obtained from the simulation of EIS data are depicted in Table 2. These values compare well with literature values [11.51–53]. During discharge at 1.5 V selected the EIS data the results are plotted as Nyquist plot ( $Z'$  vs  $Z''$ ), and are fitted by an equivalent circuit as shown in Fig. 10c.

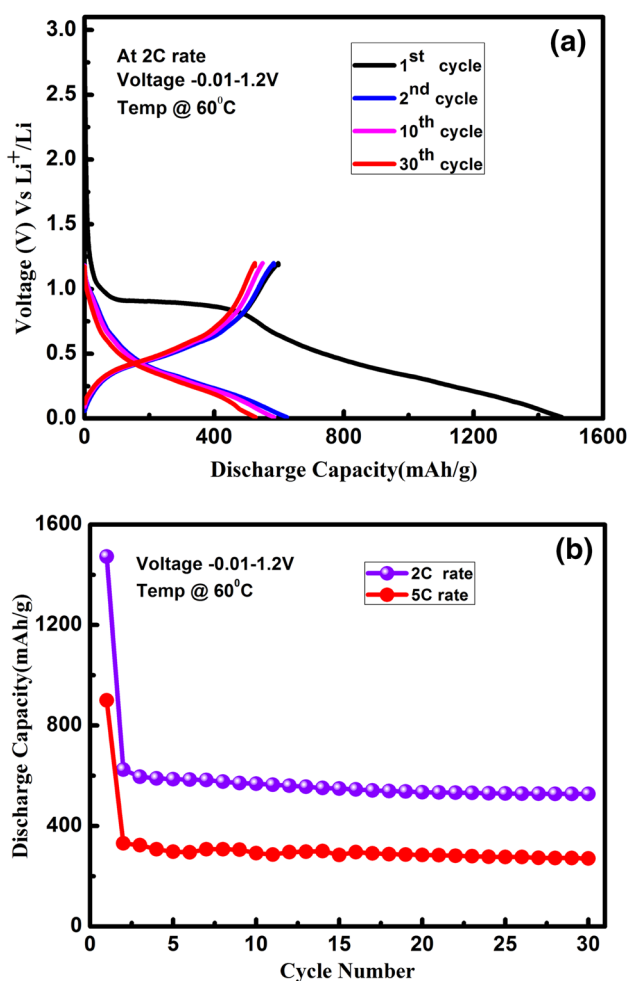
It is also useful to investigate performance of Li-ion cells at higher but safe operating temperatures (for e.g., 60 °C in our case) especially for high-power applications. It is generally understood that, at higher temperatures, the capacity fades faster and the fading rate increases with increasing temperature due to the reaction between electrolyte and electrode. So, the operating temperature is an important factor that affects the health of LIBs. From this point of view, we further investigated charge–discharge characteristics of  $\text{SnO}_2$ -carbon composite electrode at



**Fig. 10** Electrochemical impedance spectra (EIS) for  $\text{SnO}_2$ -carbon nanofiber during a, the 1st discharge at different voltage (b), enlarged view of spectra (a). c Select voltage (1.5 V) fitted with equivalent electrical circuit. Inset shows the equivalent electrical circuit used to fit the experimental impedance spectra

**Table 2** Fitted impedance values of SnO<sub>2</sub>–carbon nanofiber using equivalent electrical circuit during discharge at 2.9–0.01 V

Voltage state	$R_s$ /Ohm	$R_{sl}$ /Ohm	$R_{ct}$ /Ohm
As prepared cell (2.9 V)	5	14	39
2.0 V	14	82	$5.21E^{-06}$
1.5 V	14	65	$4.46E^{-06}$
1.0 V	14	19	$7.03E^{-06}$
0.8 V	13	10	$2.89E^{-05}$
0.6 V	13	10	$2.89E^{-05}$
0.4 V	13	9	$1.48E^{-05}$
0.2 V	13	9	$1.48E^{-05}$
0.01 V	13	9	$1.48E^{-05}$

**Fig. 11** a Charge–discharge Vs voltage curve (2C rate) at 60 °C, b cycle number Vs discharge capacity plot at 2C and 5C rate at 60 °C

60 °C. Figure 11a shows charge–discharge plots (2C rate) for SnO<sub>2</sub>–carbon nanofiber at 60 °C. Figure 11b shows the discharge capacity with respect to cycle number at 2C and

5C rates. At 2C and 5C rates, the first cycle discharge capacities are 1472 and 900 mAh/g, respectively, and 2nd cycle discharge capacities for 2C and 5C rates are 624 and 330 mAh/g, respectively. After 30 cycles, the discharge capacity for 2C and 5C rate are 527 and 270 mAh/g, respectively, with a coulombic efficiencies of about 84% for 2C, and 82% for 5C. From the above results, we can conclude that even at 60 °C SnO<sub>2</sub>–carbon composite shows desired characteristics with good capacity retention even with faster rates.

### Post cycling FESEM analysis of SnO<sub>2</sub>–carbon nanofibers

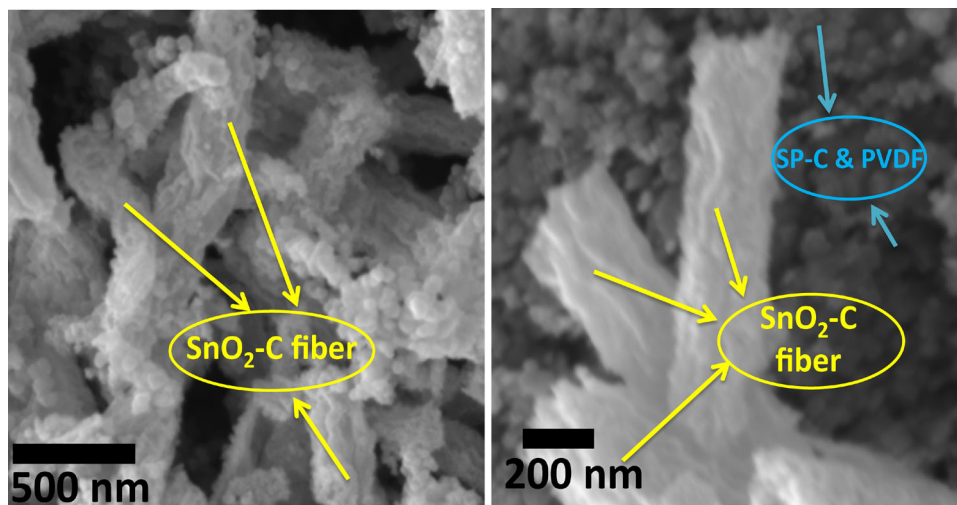
To observe the post cycling effect on the anode material, FESEM analyses were taken on the dismantled cell of these hierarchically porous SnO<sub>2</sub>–carbon nanofibers after rate capability completing 40 cycles over charge–discharge. The SnO<sub>2</sub>–carbon nanofibers can be seen in Fig. 12a, b. It also shows the presence of some particles probably of SP-C and Na-alginate binder. FESEM images prove that hierarchically porous Tin oxide–carbon nanofibers morphology is still retained even after prolonged electrochemical cycling. During the cycling SnO<sub>2</sub> nanoparticle agglomeration as well as pulverization effects are controlled by the carbon and Na-alginate binder. This hierarchically porous Tin oxide–carbon nanofibers composite with Na-alginate binder provides stronger adhesion between the electrode film and the current collector as well as uniform particle distribution of conducting networks. This could provide shorter diffusion length and good electrolyte percolation and an easy way to release the strain during cycling. Because of this the superior electrochemical performance was retained after prolonged charge–discharge cycling.

### Conclusions

Novel nanostructured SnO<sub>2</sub>–carbon composite nanofibers were in situ fabricated using the inexpensive electrospinning technique followed by thermal treatment. FESEM, HR-TEM studies reveal that nanofibers contain 4–5 nm sized interconnected nanoparticles having pores. These SnO<sub>2</sub>–carbon nanofibers exhibit high reversible capacity, excellent cyclability, and superior rate capability which are ascribed to the unique structure of the fiber mat. The hierarchical porous composite structure alleviates the issues related to the volume changes during charge–discharge resulting in good electrochemical performance even at high rates. This SnO<sub>2</sub>–carbon nanofiber composite



**Fig. 12** FESEM image of SnO<sub>2</sub>-carbon nanofibers after 40 cycles **a** at 70KX, **b** at 100KX



material delivered excellent capacity retention at 2C and 5C (84 and 82%) after 30 cycles at 60 °C.

**Acknowledgements** The authors are grateful to Director, CSIR-NPL and Director, CSIR-CECRI for their kind support and encouragements. Authors are thankful to Mr. Dinesh for TEM measurements, Mr. Jai Tawale for SEM and Dr. D.K. Misra for FESEM characterization. One of the authors, Ashish Gupta acknowledges CSIR, Govt. of India for providing Senior Research Fellowship (SRF).

**Open Access** This article is distributed under the terms of the Creative Commons Attribution 4.0 International License (<http://creativecommons.org/licenses/by/4.0/>), which permits unrestricted use, distribution, and reproduction in any medium, provided you give appropriate credit to the original author(s) and the source, provide a link to the Creative Commons license, and indicate if changes were made.

## References

- Aravindan V, Sundaramurthy J, Suresh Kumar P, Lee Y-S, Ramakrishna S, Madhavi S (2015) Electrospun nanofibers: a prospective electro-active material for constructing high performance Li-ion batteries. *Chem Commun* 51:2225–2234. doi:10.1039/c4cc07824a
- Binitha G et al (2013) Electrospun  $\alpha$ -Fe<sub>2</sub>O<sub>3</sub> nanostructures for supercapacitor applications. *J Mater Chem A* 1:11698–11704. doi:10.1039/C3TA12352A
- Bonino CA, Ji L, Lin Z, Toprakci O, Zhang X, Khan SA (2011) Electrospun carbon-tin oxide composite nanofibers for use as lithium ion battery anodes. *ACS Appl Mater Interfaces* 3:2534–2542. doi:10.1021/am2004015
- Cheng Z, Guozhao F, Caiwu L, Jiang Z, Xiaoping T, Anqiang P, Shuquan L (2016) Template-free synthesis of highly porous V<sub>2</sub>O<sub>5</sub> cuboids with enhanced performance for lithium ion batteries. *Nanotechnology* 27:305404
- Cherian CT et al (2013a) Morphologically robust NiFe<sub>2</sub>O<sub>4</sub> nanofibers as high capacity Li-ion battery anode material. *ACS Appl Mater Interfaces* 5:9957–9963. doi:10.1021/am401779p
- Cherian CT, Zheng M, Reddy M, Chowdari B, Sow CH (2013b) Zn<sub>2</sub>SnO<sub>4</sub> nanowires versus nanoplates: electrochemical performance and morphological evolution during Li-cycling. *ACS Appl Mater Interfaces* 5:6054–6060
- Deng D (2015) Li-ion batteries: basics, progress, and challenges. *Energy Sci Eng* 3:385–418. doi:10.1002/ese3.95
- Deng D, Lee JY (2008) Hollow core-shell mesospheres of crystalline SnO<sub>2</sub> nanoparticle aggregates for high capacity Li<sup>+</sup> ion storage. *Chem Mater* 20:1841–1846. doi:10.1021/cm7030575
- Dhakate SR, Gupta A, Chaudhari A, Tawale J, Mathur RB (2011) Morphology and thermal properties of PAN copolymer based electrospun nanofibers. *Synth Met* 161:411–419. doi:10.1016/j.synthmet.2010.12.019
- Dieguez A, Romano-Rodriguez A, Vila A, Morante J (2001) The complete raman spectrum of nanometric SnO<sub>2</sub> particles. *J Appl Phys* 90:1550–1557. doi:10.1063/1.1385573
- Ding S, Luan D, Boey FYC, Chen JS, Lou XWD (2011) SnO<sub>2</sub> nanosheets grown on graphene sheets with enhanced lithium storage properties. *Chem Commun* 47:7155–7157. doi:10.1039/C1CC11968K
- Ding L et al (2014) Ultrasmall SnO<sub>2</sub> nanocrystals: hot-bubbling synthesis, encapsulation in carbon layers and applications in high capacity Li-ion storage. *Sci Rep* 4:4647. doi:10.1038/srep04647
- Elizabeth I, Mathur R, Maheshwari P, Singh B, Gopukumar S (2015) Development of SnO<sub>2</sub>/multiwalled carbon nanotube paper as free standing anode for lithium ion batteries (LIB). *Electrochim Acta* 176:735–742. doi:10.1016/j.electacta.2015.06.156
- Fu Z, Li X, Xu G (2014) Novel electrospun SnO<sub>2</sub>@ Carbon Nanofibers as high performance anodes for lithium ion batteries. *Cryst Res Technol* 49:441–445. doi:10.1002/crat.201300211
- Goriparti S, Miele E, De Angelis F, Di Fabrizio E, Zaccaria RP, Capiglia C (2014) Review on recent progress of nanostructured anode materials for Li-ion batteries. *J Power Sources* 257:421–443. doi:10.1016/j.jpowsour.2013.11.103
- Gurunathan P, Ete PM, Ramesha K (2014) Synthesis of hierarchically porous SnO<sub>2</sub> microspheres and performance evaluation as Li-Ion battery anode by using different binders. *ACS Appl Mater Interfaces* 6:16556–16564. doi:10.1021/am502852x
- Hwang SM et al (2014) A case study on fibrous porous SnO<sub>2</sub> anode for robust, high capacity lithium-ion batteries. *Nano Energy* 10:53–62. doi:10.1016/j.nanoen.2014.08.020
- Jiang L-Y, Wu X-L, Guo Y-G, Wan L-J (2009) SnO<sub>2</sub>-based hierarchical nanomicrostructures: facile synthesis and their applications in gas sensors and lithium-ion batteries. *J Phys Chem C* 113:14213–14219. doi:10.1021/jp904209k
- Jibin A, Reddy M, Rao GS, Varadaraju U, Chowdari B (2012) Pb<sub>3</sub>O<sub>4</sub> type antimony oxides MSb<sub>2</sub>O<sub>4</sub> (M=Co, Ni) as anode for Li-ion

- batteries. *Electrochim Acta* 71:227–232. doi:[10.1016/j.electacta.2012.03.145](https://doi.org/10.1016/j.electacta.2012.03.145)
- Jung H-R, Lee W-J (2011) Electrochemical characterization of electrospun SnO<sub>2</sub>-embedded carbon nanofibers anode for lithium ion battery with EXAFS analysis. *J Electroanal Chem* 662:334–342. doi:[10.1016/j.jelechem.2011.09.006](https://doi.org/10.1016/j.jelechem.2011.09.006)
- Kamali AR, Divitini G, Ducati C, Fray DJ (2014) Transformation of molten SnCl<sub>2</sub> to SnO<sub>2</sub> nano-single crystals. *Ceram Int* 40:8533–8538. doi:[10.1016/j.ceramint.2014.01.067](https://doi.org/10.1016/j.ceramint.2014.01.067)
- Kim YS, Kim WB, Joo YL (2014) Further improvement of battery performance via charge transfer enhanced by solution-based antimony doping into tin dioxide nanofibers. *J Mater Chem A* 2:8323–8327. doi:[10.1039/c4ta00384e](https://doi.org/10.1039/c4ta00384e)
- Kong J, Wong SY, Zhang Y, Tan HR, Li X, Lu X (2011) One-dimensional carbon–SnO<sub>2</sub> and SnO<sub>2</sub> nanostructures via single-spinneret electrospinning: tunable morphology and the underlying mechanism. *J Mater Chem* 21:15928–15934. doi:[10.1039/C1JM12492G](https://doi.org/10.1039/C1JM12492G)
- Kong J et al (2012) Carbon/SnO<sub>2</sub>/carbon core/shell/shell hybrid nanofibers: tailored nanostructure for the anode of lithium ion batteries with high reversibility and rate capacity. *Nanoscale* 4:525–530. doi:[10.1039/c1nr10962f](https://doi.org/10.1039/c1nr10962f)
- Liu H, Huang J, Li X, Liu J, Zhang Y (2012) SnO<sub>2</sub> nanorods grown on graphite as a high-capacity anode material for lithium ion batteries. *Ceram Int* 38:5145–5149. doi:[10.1016/j.ceramint.2012.03.019](https://doi.org/10.1016/j.ceramint.2012.03.019)
- Liu L, An M, Yang P, Zhang J (2015) Superior cycle performance and high reversible capacity of SnO<sub>2</sub>/graphene composite as an anode material for lithium-ion batteries. *Scientific reports vol 5* doi:[10.1038/srep09055](https://doi.org/10.1038/srep09055)
- Lou XW, Li CM, Archer LA (2009) Designed synthesis of coaxial SnO<sub>2</sub>@ carbon hollow nanospheres for highly reversible lithium storage. *Adv Mater* 21:2536–2539. doi:[10.1002/adma.200803439](https://doi.org/10.1002/adma.200803439)
- Nithyadharseni P, Reddy M, Nalini B, Kalpana M, Chowdari B (2015) Sn-based intermetallic alloy anode materials for the application of lithium ion batteries. *Electrochim Acta* 161:261–268. doi:[10.1016/j.electacta.2015.02.057](https://doi.org/10.1016/j.electacta.2015.02.057)
- Park M-S, Kang Y-M, Wang G-X, Dou S-X, Liu H-K (2008) The effect of morphological modification on the electrochemical properties of SnO<sub>2</sub> nanomaterials. *Adv Funct Mater* 18:455. doi:[10.1002/adfm.200700407](https://doi.org/10.1002/adfm.200700407)
- Reddy MV, Subba Rao GV, Chowdari BVR (2011) Nano-(V1/2Sb1/2Sn)O<sub>4</sub>: a high capacity, high rate anode material for Li-ion batteries. *J Mater Chem* 21:10003–10011. doi:[10.1039/c0jm04140h](https://doi.org/10.1039/c0jm04140h)
- Reddy M, Subba Rao G, Chowdari B (2013a) Metal oxides and oxysalts as anode materials for Li ion batteries. *Chem Rev* 113:5364–5457. doi:[10.1021/cr3001884](https://doi.org/10.1021/cr3001884)
- Reddy M, Wei Wen BL, Loh KP, Chowdari B (2013b) Energy storage studies on InVO<sub>4</sub> as high performance anode material for Li-ion batteries. *ACS Appl Mater Interfaces* 5:7777–7785. doi:[10.1021/am401501a](https://doi.org/10.1021/am401501a)
- Reddy M, Tse LY, Bruce WKZ, Chowdari B (2015) Low temperature molten salt preparation of nano-SnO<sub>2</sub> as anode for lithium-ion batteries. *Mater Lett* 138:231–234. doi:[10.1016/j.matlet.2014.09.108](https://doi.org/10.1016/j.matlet.2014.09.108)
- Roy P, Srivastava SK (2015) Nanostructured anode materials for lithium ion batteries. *J Mater Chem A* 3:2454–2484. doi:[10.1039/C4TA04980B](https://doi.org/10.1039/C4TA04980B)
- Shengyuan Y, Peining Z, Nair AS, Ramakrishna S (2011) Rice grain-shaped TiO<sub>2</sub> mesostructures—synthesis, characterization and applications in dye-sensitized solar cells and photocatalysis. *J Mater Chem* 21:6541–6548. doi:[10.1039/C0JM04512H](https://doi.org/10.1039/C0JM04512H)
- Sivakkumar SR, Nerkar JY, Pandolfo AG (2010) Rate capability of graphite materials as negative electrodes in lithium-ion capacitors. *Electrochim Acta* 55:3330–3335. doi:[10.1016/j.electacta.2010.01.059](https://doi.org/10.1016/j.electacta.2010.01.059)
- Um JH, Yu S-H, Cho Y-H, Sung Y-E (2015) SnO<sub>2</sub> nanotube arrays embedded in a carbon layer for high-performance lithium-ion battery applications. *New J Chem* 39:2541–2546. doi:[10.1039/C4NJ01958J](https://doi.org/10.1039/C4NJ01958J)
- van Schalkwijk W, Scrosati B (2007) *Advances in lithium-ion batteries*. Springer, Heidelberg
- Viet AL, Reddy M, Jose R, Chowdari B, Ramakrishna S (2009) Nanostructured Nb<sub>2</sub>O<sub>5</sub> polymorphs by electrospinning for rechargeable lithium batteries. *J Phys Chem C* 114:664–671. doi:[10.1021/jp9088589](https://doi.org/10.1021/jp9088589)
- Wang M, Li S, Zhang Y, Huang J (2015) Hierarchical SnO<sub>2</sub>/carbon nanofibrous composite derived from cellulose substance as anode material for lithium-ion batteries chemistry–A. *Eur J* 21:16195–16202
- Wang S-X, Yap CC, He J, Chen C, Wong SY, Li X (2016) Electrospinning: a facile technique for fabricating functional nanofibers for environmental applications. *Nanotechnol Rev* 5:51–73. doi:[10.1515/ntrev-2015-0065](https://doi.org/10.1515/ntrev-2015-0065)
- Wu Y-P, Rahm E, Holze R (2003) Carbon anode materials for lithium ion batteries. *J Power Sources* 114:228–236. doi:[10.1016/S0378-7753\(02\)00596-7](https://doi.org/10.1016/S0378-7753(02)00596-7)
- Wu Y, Balakrishna R, Reddy M, Nair AS, Chowdari B, Ramakrishna S (2012) Functional properties of electrospun NiO/RuO<sub>2</sub> composite carbon nanofibers. *J Alloy Compd* 517:69–74. doi:[10.1016/j.jallcom.2011.12.019](https://doi.org/10.1016/j.jallcom.2011.12.019)
- Xia W et al (2012) Facile approach to synthesize SnO<sub>2</sub> nanoparticles@ carbon nanofibers as anode materials for lithium-ion battery. *J Power Sources* 217:351–357. doi:[10.1016/j.jpowsour.2012.05.072](https://doi.org/10.1016/j.jpowsour.2012.05.072)
- Xia X, Li S, Wang X, Liu J, Wei Q, Zhang X (2013) Structures and properties of SnO<sub>2</sub> nanofibers derived from two different polymer intermediates. *J Mater Sci* 48:3378–3385. doi:[10.1007/s10853-012-7122-7](https://doi.org/10.1007/s10853-012-7122-7)
- Yang T, Lu B (2014) Highly porous structure strategy to improve the SnO<sub>2</sub> electrode performance for lithium-ion batteries. *Phys Chem Chem Phys* 16:4115–4121. doi:[10.1039/C3CP54144D](https://doi.org/10.1039/C3CP54144D)
- Yang Z et al (2010) Easy preparation of SnO<sub>2</sub>@ carbon composite nanofibers with improved lithium ion storage properties. *J Mater Res* 25:1516–1524. doi:[10.1557/JMR.2010.0194](https://doi.org/10.1557/JMR.2010.0194)
- Yang Q, Zhao J, Sun T, Yu J (2015) Enhanced performance of SnO<sub>2</sub>-C composite fibers containing NiO as lithium-ion battery anodes. *Ceram Int* 41:11213–11220. doi:[10.1016/j.ceramint.2015.05.071](https://doi.org/10.1016/j.ceramint.2015.05.071)
- Yim C-H, Baranova EA, Courtel FM, Abu-Lebdeh Y, Davidson IJ (2011) Synthesis and characterization of macroporous tin oxide composite as an anode material for Li-ion batteries. *J Power Sources* 196:9731–9736. doi:[10.1016/j.jpowsour.2011.07.061](https://doi.org/10.1016/j.jpowsour.2011.07.061)
- Zhang Y, Jiang L, Wang C (2015) Facile synthesis of SnO<sub>2</sub> nanocrystals anchored onto graphene nanosheets as anode materials for lithium-ion batteries. *Phys Chem Chem Phys* 17:20061–20065. doi:[10.1039/C5CP03305E](https://doi.org/10.1039/C5CP03305E)
- Zhou X, Dai Z, Liu S, Bao J, Guo YG (2014) Ultra uniform SnO<sub>2</sub>/carbon nanohybrids toward advanced lithium ion battery anodes. *Adv Mater* 26:3943–3949. doi:[10.1002/adma.201400173](https://doi.org/10.1002/adma.201400173)
- Zhou B et al (2015) Amorphous carbon framework stabilized SnO<sub>2</sub> porous nanowires as high performance Li-ion battery anode materials RSC. *Advances* 5:49926–49932. doi:[10.1039/C5RA05372B](https://doi.org/10.1039/C5RA05372B)
- Zhu X, Zhu Y, Murali S, Stoller MD, Ruoff RS (2011) Reduced graphene oxide/tin oxide composite as an enhanced anode material for lithium ion batteries prepared by homogenous coprecipitation. *J Power Sources* 196:6473–6477. doi:[10.1016/j.jpowsour.2011.04.015](https://doi.org/10.1016/j.jpowsour.2011.04.015)
- Zhu P, Wu Y, Reddy M, Nair AS, Chowdari B, Ramakrishna S (2012) Long term cycling studies of electrospun TiO<sub>2</sub> nanostructures and their composites with MWCNTs for rechargeable Li-ion batteries RSC. *Advances* 2:531–537. doi:[10.1039/C1RA00514F](https://doi.org/10.1039/C1RA00514F)